BL33XU
TOYOTA

1. Introduction

BL33XU was constructed in FY2009 and is operated by Toyota Central R&D Labs [1]. It was originally designed to perform quick-scanning X-ray absorption spectroscopy (QXAFS) for *operando* analysis and three-dimensional X-ray diffraction (3DXRD), which were unavailable at SPring-8 before 2009. Currently, the beamline is equipped with instrumentation for small-angle X-ray scattering (SAXS), X-ray diffraction (XRD) with a multi-axis goniometer, and X-ray computed tomography (CT) and laminography (Fig. 1). This report details the current status and recent technological progress of the beamline in FY2019.

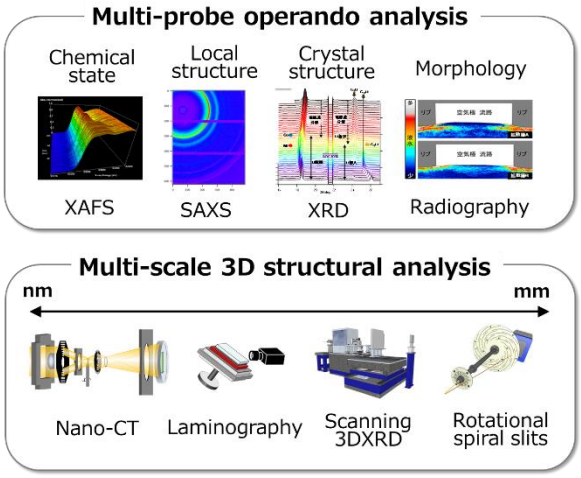

Fig. 1. Analysis techniques at BL33XU.

2. BL33XU beamline

2-1. Beamline layout

BL33XU is a medium-length beamline, and has an experimental facility building outside the storage ring building. An optics hutch is located in the storage ring building, and three experimental hutches (EH1–3), a chemical laboratory, and an office room constitute the experimental facility building.

Figure 2 shows the layout of the optical components of the beamline. The beamline has two optics with different types of monochromators. Optics 1 consists of horizontal deflection mirrors (M1 and M2) in the optics hutch, compact monochromators (C-Mono) with channel-cut crystals, and vertical deflection mirrors (M3 and M4) in EH1. Optics 1 is mainly used for QXAFS analysis. Optics 2 is composed of a double-crystal monochromator (SPring-8 standard type), vertical deflection mirrors (M4 and M5), and Kirkpatrick-Baez (KB) focusing mirrors. A 1-μm-square 50-keV microbeam is available at EH3.

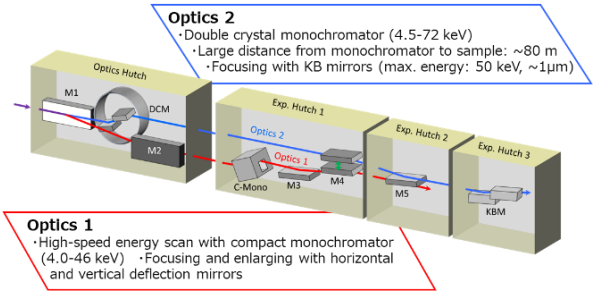

Fig. 2. Optical components of BL33XU.

2-2. Analysis techniques

(1) QXAFS

Rapid acquisition of XAFS data with a temporal resolution of up to 10 ms is realized by combining a servo-motor–driven channel-cut monochromator with a tapered undulator [2]. Two monochromators with Si(111) and Si(220) crystals cover an energy range 4.0–45 keV. Various *in situ* measurement techniques using the QXAFS system have been developed. These include simultaneous XAFS and

XRD measurements of the positive and negative electrodes of lithium-ion batteries during charging and discharging [3].

(2) SAXS

For SAXS, a PILATUS 300K (Dectris) detector is available and the camera length can be varied from tens of centimeters to 4.5 meters. Several *in situ* observation techniques using SAXS were developed. For example, the structural evolution of resins during injection molding can be analyzed [4].

(3) XRD

A multi-axis goniometer system was developed to measure the internal stresses and strains of the mechanical and electronic components for reliability analysis. A newly developed rotating and revolving spiral slit system was installed in the goniometer system to detect diffraction from microregions in components with a two-dimensional PILATUS detector. Rotating shield disks with unique spiral-shaped slits enable depth-resolved strain distribution measurements [5].

(4) Scanning 3DXRD

The scanning 3DXRD method was developed for non-destructive analysis of metallic materials with hundreds of grains in the observation region. In 2013, this method was validated, and high-resolution analysis using a high-energy microbeam was demonstrated in 2015 [6]. This method can acquire the average properties of each grain and the spatial distribution of the properties in the grain. Hence, the strain distribution in a grain and information on the crystal rotation associated with plastic deformation can be obtained [7].

(5) X-ray CT and laminography

X-ray CT and laminography techniques were introduced to meet the growing demand for high-resolution, non-destructive structural analysis of materials. A resolution less than 1 μm was achieved for the CT method, and a ~1-μm resolution was recently obtained in the laminography method. In addition, an imaging CT system with a Fresnel zone plate (FZP) was installed in 2017, which achieved a resolution of ~100 nm.

3. Recent technological progress: Observations of dynamic behavior of liquid water in gas diffusion layer of polymer electrolyte fuel cells

In polymer electrolyte fuel cells (PEFCs), water is generated on the cathode side of a membrane-electrode assembly (MEA) during power generation (Fig. 3). Most of the generated water is discharged to the flow channel in the gas or liquid form (hereinafter referred to as water) through the gas diffusion layer (GDL). A flooding phenomenon, where a large amount of water remains in the cathode GDL during high-load operation, inhibits the diffusion of oxygen gas into the catalyst layer, resulting in a decreased power generation performance. To improve the power output of the

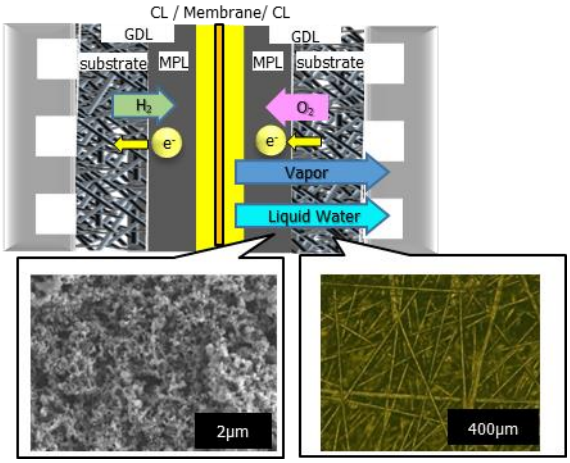

Fig. 3. (top) Schematic diagram of a polymer electrolyte fuel cell (PEFC). (bottom left) SEM image of a micro porous layer (MPL). (bottom right) Optical microscope image of a substrate.

fuel cell, both water drainage and oxygen gas diffusion in the GDL must be optimized.

The GDL consists of a substrate layer and a hydrophobic microporous layer (MPL). The substrate is made of carbon fiber and a binder. It has pore structures of tens to hundreds of μm. For the substrate, the dynamic behavior of water during power generation was visualized three-dimensionally by *operando* X-ray micro-CT measurements [8-10]. The MPL consists of electron-conducting nano-scale carbon and polytetrafluoroethylene (PTFE) with pore structures of tens to hundreds of nm. The behavior of water in the MPL, which is close to the catalyst layer, is not well understood because the high X-ray absorption of platinum in the catalyst layer makes X-ray CT measurements difficult for the adjacent MPL.

In this study, X-ray micro-CT measurements were made by injecting water into the GDL to investigate the behavior of the water in the MPL. X-ray CT can be measured without a catalyst layer by simulating the power generation state with water injection. An MPL with relatively large pore structures of tens to hundreds of μm was observed. X-rays were monochromatized at 14 keV using a standard monochromator, and 600 transmission images were acquired while rotating the sample 180° in 4.2 s. An X-ray camera with a pixel size of 0.65 μm × 0.65 μm as used as the detector. Three-dimensional reconstruction was performed using the software [11,12].

The X-ray CT results showed that the MPL was mainly composed of small pores of ~30 μm and large pores of ~100 μm. Figure 4 shows the 3D structure of the region containing the small pores and their temporal evolution during water injection. For the small pores, only certain pores were filled

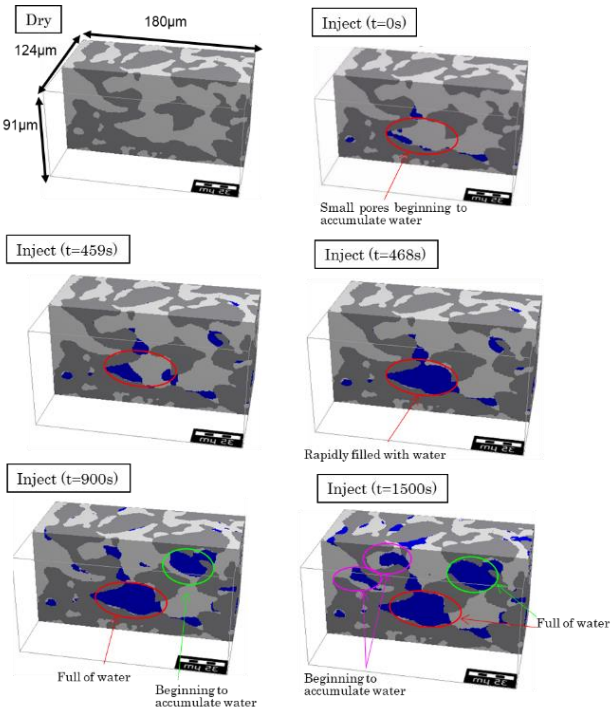

Fig. 4. 3D images of small pores (~30 μm) and their temporal evolution. Light gray: pores, dark gray: MPL materials, blue: water.

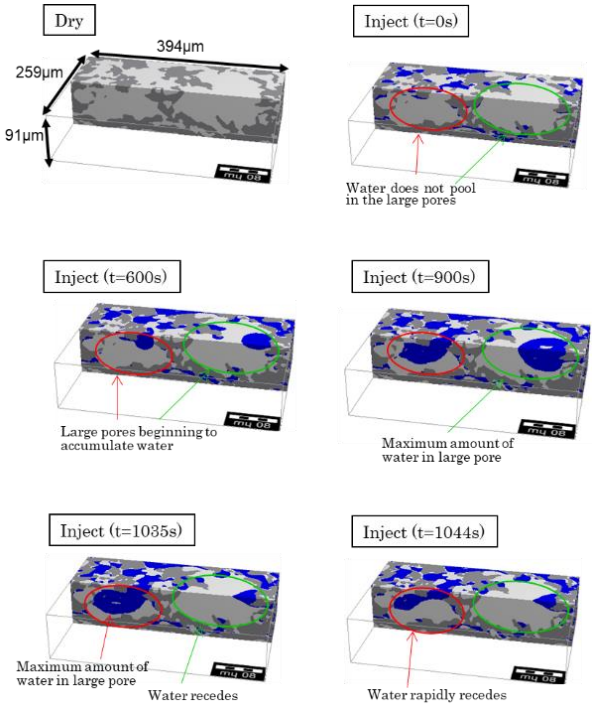

Fig. 5. 3D images of large pores (~100 μm) and their temporal evolution. Light gray: pores, dark gray: MPL materials, blue: water.

with water, but then the amount of water in the other pores increased.

Figure 5 shows the temporal evolution of the 3D structure of the region containing the large pores. Immediately after the water injection, water accumulated in the small pores around the large pores; later, water accumulated in the large pores, but they did not reach saturation. Subsequently, the amount of water in the large pores decreased rapidly.

Figure 6 shows the temporal evolution of the water saturation rate obtained from the 3D images in Figs. 4 and 5. The water saturation rate at the small pores monotonically increased while the water saturation rate of the large pores showed an oscillating trend between 25% and 35%. Several such oscillations were observed, which may reflect the water movement pattern in the MPL.

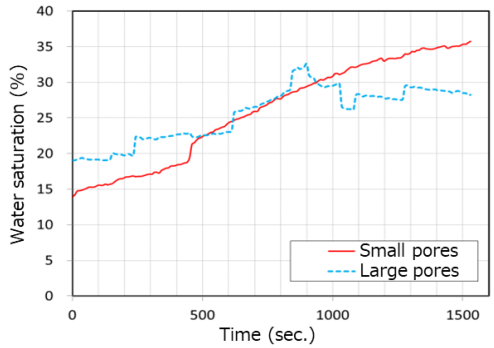

Fig. 6. Water saturation obtained from Figs. 4 and 5.

Takamasa Nonaka and Satoshi Yamaguchi
Toyota Central R&D Labs

References:

[1] Nonaka, T. et al. (2016). *AIP Conf. Proc.,* 1741, 030043,

[2] Nonaka, T. et al. (2012). *Rev. Sci. Instrum.,* 83, 083112.

[3] Makimura Y. et al. (2016). *J. Electrochem. Soc.* 163(7), A1450-A1456.

[4] Harada, M. et al. (2015). *SPring-8 User Experiment Report*, 2015A7003, 2015B7003.

[5] Setoyama, D. et al. (2015). *Proc. MECASENSE 2015*, 4.

[6] Hayashi, Y. et al. (2017). *SPring-8 User Experiment Report*, 2017A7002, 2017B7002.

[7] Hayashi, Y. et al. (2019). *Science*, 366, 1492-1496.

[8] Eller, J. et al. (2017). *J. Electrochem. Soc.,* 164(2), F115-F126.

[9] Eller, J. et al. (2011). *J. Electrochem. Soc.,* 158(8), B963-B970.

[10] Nagai, Y. et al. (2019). *J. Power Sources,* 435, 226809.

[11] Uesugi, K. et al. (2010). *AIP Conf. Proc*., 1266, 47-50.

[12] Suzuki, Y. et al. (2002). *J. Synchrotron Rad.,* 9, 160-165.